Elastoplastic analysis of compact and thin-walled structures using classical and refined beam finite element models

Elastoplastic analysis of compact and thin walled structures using classical and refined beam finite element models

E. Carrera*, I. Kaleel†, M. Petrolo‡
Department of Mechanical and Aerospace Engineering, Politecnico di Torino,
Corso Duca degli Abruzzi 24, 10129 Torino, Italy

Submitted to Mechanics of Advanced Materials and Structures

Author for correspondence:
E. Carrera, Professor of Aerospace Structures and Aeroelasticity,
Department of Mechanical and Aerospace Engineering,
Politecnico di Torino,
Corso Duca degli Abruzzi 24,
10129 Torino, Italy,
tel: +39 011 090 6836,
fax: +39 011 090 6899,
e-mail: erasmo.carrera@polito.it

*Professor of Aerospace Structures and Aeroelasticity, e-mail: erasmo.carrera@polito.it
†Ph.D. Student, e-mail: ibrahim.kaleel@polito.it
‡Assistant Professor, e-mail: marco.petrolo@polito.it

Abstract

The paper presents results on the elastoplastic analysis of compact and thin walled structures via refined beam models. The application of Carrera Unified Formulation (CUF) to perform elastoplastic analysis of isotropic beam structures is discussed. Particular attention is paid to the evaluation of local effects and cross-sectional distortions. CUF allows formulation of the kinematics of a one-dimensional (1D) structure by employing a generalized expansion of primary variables by arbitrary cross-section functions. Two types of cross-section expansion functions, TE (Taylor Expansion) and LE (Lagrange Expansion), are used to model the structure. The isotropically work-hardening von Mises constitutive model is incorporated to account for material non-linearity. A Newton-Raphson iteration scheme is used to solve the system of nonlinear algebraic equations. Numerical results for compact and thin walled beam members in plastic regime are presented with displacement profiles and beam deformed configurations along with stress contour plots. The results are compared against classical beam models such as Euler-Bernoulli Beam Theory (EBBT) and Timoshenko Beam Theory (TBT), reference solutions from literature, and three-dimensional (3D) solid finite element models. The results highlight: 1. the capability of the present refined beam models to describe the elastoplastic behavior of compact and thin walled structure with 3D-like accuracy; 2. local effects and severe cross-sectional distortions can be detected; 3. the computational cost of the present modeling approach is significantly lower than shell and solid model ones.

Keywords: CUF, Beam, Plasticity, Refined models, Thin walled structures

1 Introduction

To maximize the capabilities of high-performance metallic structures, it is important to understand the physical nonlinearity encompassed within the structural system, and detect local, 3D deformation and stress states under complex loading conditions. Non-linear simulation is a necessary tool for a structural designer, especially to capture the design limits of the system. As non-linear analysis requires accurate descriptions of displacement and stress states, designers often resort to 3D finite element simulation to obtain a reasonable structural response. In the case of thin walled structures, shell finite element analysis is also widely adopted. Computational costs often overshadow the effectiveness of such approaches. Thus, such simulations pose accuracy versus computational cost trade-off.

The present paper deals with physically non-linear finite element simulations of metallic structures via refined beam models. The finite element framework is based on the computationally efficient Carrera Unified Formulation (CUF)[1]. Particular attention is paid to thin walled structures and localized phenomena. A brief overview of the most common approaches for the elastoplastic analysis of metallic, thin walled structures via beam elements is given hereinafter.

Over the past few decades, there have been numerous efforts towards developing computationally efficient physically non-linear simulation frameworks for slender structural members, with particular attention paid to frames. Due to significant computational demands, these simulation frameworks often resort to analytical formulations [2], or simplified numerical approaches such as plastic zone method and plastic hinge method [3–8], which limits the kind of problems that can be analyzed. Timoshenko and Gere reported a theoretical formulation for inelastic beams [2]. The principal limitations of the formulation were that formulation neglected shear effects and valid only for beams with a doubly-symmetric cross-section. Elastic treatment of shear stress components can also be found in [7]. In the plastic zone method, the structural members are discretized via finite elements, and the cross-section is subdivided into fibers. The residual stress in each fiber is assumed to be constant. A large number of cross-section fibers can be necessary to obtain accurate response [9]. The plastic hinge method is an efficient alternative to the plastic zone method. The methodology is based on concentrated plasticity, where plastic hinges are used to model inelasticity. Mata et al. developed a geometrically nonlinear formulation for beams under the assumption of planarity of cross-section [4].

Recently, the attention has been paid to the use of beam models to deal with the elastoplastic analysis of thin walled structures. In particular, remarkably progresses were made through the Generalized Beam Theory (GBT) [10–12]. Via the GBT, local plasticity and cross-section distortions of thin walled members can be detected accurately, and with low computational costs.

In the present paper, a generalized framework is proposed for physically non-linear analysis of both compact and thin walled metallic structures. The formulation is based on a class of refined 1D beam models called Carrera Unified Formulation (CUF) [1]. CUF is a hierarchical framework that enables one to develop a 1D displacement field in a kinematically enriched manner. The differential equations are formulated via a few fundamental nuclei,

which are independent of the theory order or cross-section geometry. 1D CUF models were originally developed for expansion functions based on Taylor series, where theory order of the model is a free parameter [13]. Carrera and Petrolo introduced a new class of expansion functions based on Lagrange-type polynomials, which can handle local cross-section deformations very efficiently [14]. LE models allow representing every part of a multi-component structure via 1D finite element, leading to Component-Wise (CW) approach. CW approach can use the same 1D FE for different components of structures, thereby reducing the computational effort [15]. Therefore, CUF can deal with arbitrary cross-sections, various classes of material models and boundary conditions, without any ad-hoc assumptions. Over the last couple of decades, 1D CUF models have been successfully employed to deal with wide range of structural problems such as static and free vibration analysis of thin walled structures[16], buckling of thin walled composite beams [17] and laminated composite beam structures [18]. Recently, Pagani and Carrera developed a geometrically nonlinear finite element framework based on CUF [19]. Various numerical assessments including large deflection analysis, buckling and post-buckling of slender compact cross-section beams and thin walled structures were reported. In [20], Carrera et al. presented an extended review of recent developments in refined theories for beam based on CUF and its extensive applications in diverse fields. 2D CUF models have also been successfully employed to undertake a diverse range of problems for plates and shells [21].

This paper extends the enhanced capabilities of 1D CUF models for physically non-linear finite element simulation. The J_2-flow theory is utilized to model the plastic behavior [22]. Computationally efficient non-linear 1D CUF framework is introduced. In Section 2, a brief introduction to CUF models is given. Two classes of expansion function are also illustrated in detail. The finite element formulations for the CUF model is described in Section 3. Linearized incremental framework along with numerical aspects of plasticity model is also discussed. Section 4 contains the numerical examples of compact and thin walled beams. All the results are validated against with 3D finite element solution from ABAQUS. Convergence study is also undertaken. The section discusses in detail the accuracy and computational efficiency of CUF models. Finally, the conclusions are drawn in Section 5.

2 Carrera Unified Formulation

Carrera Unified Formulation (CUF) is a hierarchical scheme leading to a refined structural theory. In contrast to the classical beam models such as Euler-Bernoulli Beam Theory (EBBT) and Timoshenko Beam Theory (TBT), CUF defines the kinematic field in a unified manner. Based on the coordinate system defined in Fig. 1, the kinematics of a CUF beam model can be expressed as follows:

$$\mathbf{u} = F_\tau(x, z)\, \mathbf{u}_\tau(y), \qquad s = 1, 2, ...M \tag{1}$$

Where F_τ is the cross-section expansion function, $\mathbf{u}_\tau(y)$ is the generalized displacement vector and M indicates the number of expansion terms. The choice of F_τ and number of terms M are arbitrary. Therefore, formulation of kinematic field as expressed in Eq. 1 gives freedom to adopt different kind of expansion functions. Two classes of functions are described in the following paper: (1) Taylor Expansion (TE) and (2) Lagrange Expansion (LE).

2.1 Taylor Expansion

Taylor Expansion (TE) models are formulated employing polynomial expansion of the kind $x^i z^j$ as cross-section function F_τ. TE model for a rectangular cross-section beam is illustrated in Fig. 5. For instance, a second order (N=2) TE model can be expressed as follows:

$$u_x = u_{x_1} + x\, u_{x_2} + z\, u_{x_3} + x^2\, u_{x_4} + xz\, u_{x_5} + z^2\, u_{x_6} \tag{2a}$$

$$u_y = u_{y_1} + x\, u_{y_2} + z\, u_{y_3} + x^2\, u_{y_4} + xz\, u_{y_5} + z^2\, u_{y_6} \tag{2b}$$

$$u_z = u_{z_1} + x\, u_{z_2} + z\, u_{z_3} + x^2\, u_{z_4} + xz\, u_{z_5} + z^2\, u_{z_6} \tag{2c}$$

The model above consists of a constant, linear and quadratic term in the cross-section expansion. It should be noted that the order N of the expansion is a user input and it determines the theory of the beam. Classical beam theories such as EBBT and TBT can be obtained as special cases of linear TE model (N=1). For further reading, refer to the original paper on TE CUF models by Carrera and Giunta [13].

2.2 Lagrange Expansion

Lagrange Expansion (LE) models are formulated using Lagrange polynomials as cross-section function F_τ. LE models are characterized by purely displacement variables whereas TE models consist of displacement and N-order derivatives as unknown variables. Lagrange elements can be used to model arbitrary cross-section geometry by adopting an iso-parametric formulation. In this paper, bi-quadratic nine-node Lagrange polynomials (L9) are employed. The displacement field within an L9 element can be expressed as:

$$u_x = F_1(x,z)\, u_{x_1}(y) + F_2(x,z)\, u_{x_2}(y) + F_3(x,z)\, u_{x_3}(y) + ... + F_9(x,z)\, u_{x_9}(y) \tag{3a}$$

$$u_y = F_1(x,z)\, u_{y_1}(y) + F_2(x,z)\, u_{y_2}(y) + F_3(x,z)\, u_{y_3}(y) + ... + F_9(x,z)\, u_{y_9}(y) \tag{3b}$$

$$u_z = F_1(x,z)\, u_{z_1}(y) + F_2(x,z)\, u_{z_2}(y) + F_3(x,z)\, u_{z_3}(y) + ... + F_9(x,z)\, u_{z_9}(y) \tag{3c}$$

Where u_{x_1},.....,u_{z_9} are the translational degrees of freedom of the L9 element and F_1,.....,F_9 are the Lagrange interpolation functions. The beam can be further refined by discretizing the cross-section with multiple L-elements. LE leads to FE mathematical models built by using only physical boundaries; artificial lines (beam axes) and surfaces (plate/shell reference surfaces) are no longer necessary. Also, each L-element retains its

material characteristics. The homogenization takes place only at the interface level. More information on LE based CUF models can be found in the original paper by Carrera and Petrolo [14].

3 Finite Element Formulation

3.1 Preliminaries

The coordinate system of the beam is illustrated in Fig. 1. The longitudinal axis of the beam coincides with the coordinate y ($0 \leq y \leq L$) and the cross-section Ω is overlayed on the x-z plane. The displacement vector is

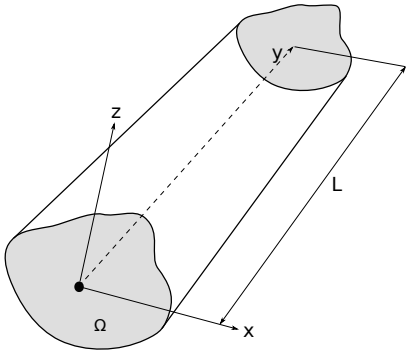

Figure 1: Generic beam model with the Cartesian reference system

given by

$$\mathbf{u}(x, y, z) = \{u_x \; u_y \; u_z\}^T \tag{4}$$

The stress, $\boldsymbol{\sigma}$, and strain, $\boldsymbol{\epsilon}$, are grouped as follows:

$$\boldsymbol{\sigma} = \{\sigma_{xx} \; \sigma_{yy} \; \sigma_{zz} \; \sigma_{xy} \; \sigma_{xz} \; \sigma_{yz}\}^T, \qquad \boldsymbol{\epsilon} = \{\epsilon_{xx} \; \epsilon_{yy} \; \epsilon_{zz} \; \epsilon_{xy} \; \epsilon_{xz} \; \epsilon_{yz}\}^T \tag{5}$$

With small strain assumptions, the linear strain-displacement relation is given by:

$$\boldsymbol{\epsilon} = \mathbf{D} \, \mathbf{u} \tag{6}$$

Where $\mathbf{D}$ is the linear differential operator on $\mathbf{u}$ and is given by:

$$\mathbf{D} = \begin{bmatrix} \frac{\partial}{\partial x} & 0 & 0 \\ 0 & \frac{\partial}{\partial y} & 0 \\ 0 & 0 & \frac{\partial}{\partial z} \\ \frac{\partial}{\partial y} & \frac{\partial}{\partial x} & 0 \\ \frac{\partial}{\partial z} & 0 & \frac{\partial}{\partial x} \\ 0 & \frac{\partial}{\partial z} & \frac{\partial}{\partial y} \end{bmatrix} \tag{7}$$

In case of linear elastic material, stress can be related to strain through the relation

$$\boldsymbol{\sigma} = \mathbf{C}\boldsymbol{\epsilon} \tag{8}$$

Where $\mathbf{C}$ is the elastic material matrix. In Section 3.3, more details on the elasto-plastic constitutive matrix is discussed. The beam is desctrized using the classical finite element technique, where the displacement vector is given by

$$\mathbf{u}(x, y, z) = F_\tau(x, z)N_i(y)\mathbf{u}_{\tau i} \tag{9}$$

Where N_j stands for the shape function, F_s for the cross-section expansion function and $\mathbf{u}_{\tau i}$ for nodal solution vector,

$$\mathbf{u}_{\tau i} = [u_{x_{\tau i}}\ u_{y_{\tau i}}\ u_{z_{\tau i}}]^T \tag{10}$$

Three types of beam elements are employed, B2 (two nodes), B3(three nodes) and B4 (four nodes), which stands for linear, quadratic and cubic approximation respectively. For the sake of brevity, the shape functions are not reported here. They can be found in the book by Bathe [23]. As discussed in Section 2, cross-section is defined using two classes of function: (1) Taylor Expansion (TE) and (2) Lagrange Expansion (LE). The choice of cross-section discretization for LE class (i.e. type, number, and distribution of cross-section) or theory order N for TE class, is independent of the choice of the beam finite elements.

The stiffness matrix and the external load vector of the elements can be obtained by mean of the Principle of Virtual Displacements

$$\delta L_{int} - \delta L_{ext} = 0 \tag{11}$$

Where L_{int} stands for internal strain energy and is given by:

$$\delta L_{int} = \int_V (\delta\boldsymbol{\epsilon}\ \boldsymbol{\sigma})dV \tag{12}$$

and L_{ext} stands for work due to external loading and can formulated as:

$$L_{ext} = F_s N_j \delta\mathbf{u}_{sj}^T\mathbf{P} \tag{13}$$

Where $\mathbf{P}$ is the generic nodal force vector. Using Eqs. 8, 9 and 12, the virtual variation of internal strain energy can be reformulated as

$$\delta L_{int} = \delta\mathbf{u}_{sj}^T\mathbf{K}_{ij\tau s}\mathbf{u}_{\tau i} \tag{14}$$

Where $\mathbf{K}_{ij\tau s}$ is the 3 x 3 stiffness matrix termed as fundamental nucleus (FN). The explicit expressions for nine components of the fundamental nucleus is not repeated here, but it is given in [1], with detailed information on CUF.

3.2 Non-linear incremental framework

The incremental equilibrium equation formulated is based on the Principle of Virtual Work as given in Eq. 11. Using Eqns. 11, 13 and 14, the equilibrium can be expressed in a unified manner as follows:

$$\mathbf{K}^{S}_{ij\tau s}\mathbf{u}_{\tau i} - \mathbf{p}_{\tau i} = 0 \tag{15}$$

Where $\mathbf{K}^{S}_{ij\tau s}$ and $\mathbf{p}_{\tau i}$ are the Fundamental Nuclei of the secant stiffness matrix and the external load vector respectively and $\mathbf{u}_{\tau i}$ is the unknown vector. Equation 15 represents a set of three algebraic equations. The derivation of fundamental nuclei of stiffness matrix and nodal load vector is not reported here but can be found in [1]. According to CUF, the finite element governing equations of a generic, arbitrary higher-order model can be obtained by expanding Eq. 15 with the FNs using the indices $\tau, s = 1, ...M$ and $i, j = 1, ..., p+1$ is given as follows

$$\mathbf{K}^{S}\mathbf{u} - \mathbf{p} = 0 \tag{16}$$

Where $\mathbf{K}^{S}$,$\mathbf{u}$ and $\mathbf{p}$ are the global assembled finite element arrays for the structural system. Additional information of finite element assembly of the FNs can be found in the book by Carrera et al [1].
In the current work, the external load application control is realized by parametrisation of external load vector with load parameter λ. Therefore,the equilibrium equation can be reformulated as

$$\mathbf{r}(\mathbf{u}) - \lambda_n \mathbf{p} = 0 \quad n \in [0, NT] \tag{17}$$

Where λ is applied step-wise to discretize the solution and is analogous to time steps of transient problems, n is the step index and NT is the total number of steps. An equilibrium state at step n is characterized with an internal force vector $\mathbf{r}_n$, solution vector $\mathbf{u}_n$ and external load vector $\mathbf{p}_n$ ($\mathbf{p}_n = \lambda_n \mathbf{p}$). The step-wise numerical solution from an equilibrium point n to n+1 is accomplished through Newton-Raphson scheme. A schematic representation of a load-controlled Newton-Raphson scheme (or tangent method) is illustrated in Fig. 2. The

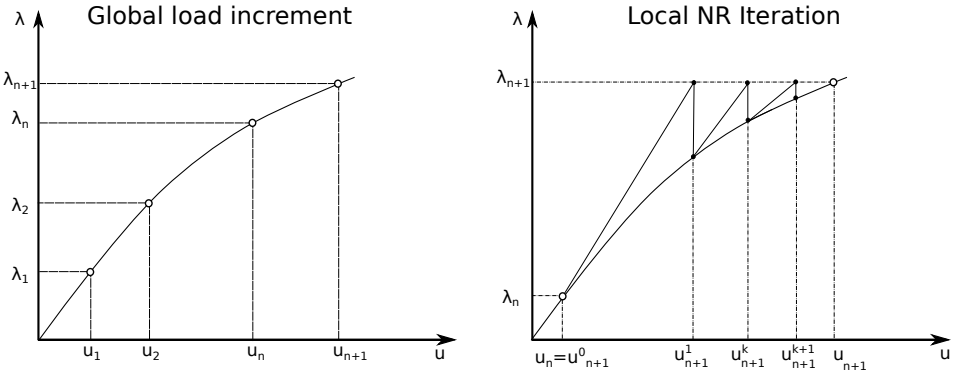

Figure 2: 1D representation of Newton-Raphson iterative method with load control

Taylor series expansion of the internal force vector determined by the solution vector $\mathbf{u}_{n+1}^k$ is given by

$$\mathbf{r}(\mathbf{u}_{n+1}^{k+1}) = \mathbf{r}(\mathbf{u}_{n+1}^k) + \frac{\partial \mathbf{r}(\mathbf{u}_{n+1}^k)}{\partial \mathbf{u}_{n+1}^k}(\mathbf{u}_{n+1}^{k+1} - \mathbf{u}_{n+1}^k) + \frac{1}{2}\frac{\partial^2 \mathbf{r}(\mathbf{u}_{n+1}^k)}{\partial \mathbf{u}_{n+1}^{k\,2}}(\mathbf{u}_{n+1}^{k+1} - \mathbf{u}_{n+1}^k)^2 + ... \tag{18}$$

Where k stands for the iteration index within a load step. The Newton-Raphson system is formulated by truncating the Taylor series expansion at the linear term:

$$\mathbf{r}(\mathbf{u}_{n+1}^{k+1}) = \mathbf{r}(\mathbf{u}_{n+1}^k) + \frac{\partial \mathbf{r}(\mathbf{u}_{n+1}^k)}{\partial \mathbf{u}_{n+1}^k}\Delta\mathbf{u} \qquad \Delta\mathbf{u} = \mathbf{u}_{n+1}^{k+1} - \mathbf{u}_{n+1}^k \tag{19}$$

The partial derivative of the current internal vector force with respect to the actual solution state $\mathbf{u}_{n+1}^k$ is termed as the tangent stiffness matrix $\mathbf{K}_T$. Therefore, Eq. 19 can be written as

$$\mathbf{r}(\mathbf{u}_{n+1}^{k+1}) = \mathbf{r}(\mathbf{u}_{n+1}^k) = \mathbf{K}_T(\mathbf{u}_{n+1}^k)\Delta\mathbf{u} \qquad \Delta\mathbf{u} = \mathbf{u}_{n+1}^{k+1} - \mathbf{u}_{n+1}^k \tag{20}$$

In general, tangent stiffness matrix is obtained by taking variations of integrated equations with respect to solution variables. Since the current work takes into account only material nonlinearity with small strain assumption, the computation of tangent stiffness matrix is reduced to obtaining the material tangent matrix. The numerical implementation of the elastoplastic consistent tangent matrix is discussed in 3.3.1.

3.3 Numerical aspects of plasticity model

The following section describes the numerical aspects of the J_2 flow theory (von Mises) implemented in the current context. The von Mises theory is based on the hypothesis that metal yields when the J_2 stress deviator reaches the critical value. This condition is represented for an isotropic hardening case in Eq. 21,

$$f = q(\boldsymbol{\sigma}) - \sigma_y(\bar{\epsilon}_p) \tag{21}$$

with

$$q(\boldsymbol{\sigma}) = \sqrt{-3J_2} = \sqrt{\frac{1}{2}\left[(\sigma_{xx} - \sigma_{yy})^2 + (\sigma_{yy} - \sigma_{zz})^2 + (\sigma_{zz} - \sigma_{xx})^2 + 6(\sigma_{xy}^2 + \sigma_{xz}^2 + \sigma_{yz}^2)\right]} \tag{22}$$

Where f is the von Mises yield locus, $q(\boldsymbol{\sigma})$ is the von Mises stress, σ_y is the yield stress (elastic limit), J_2 is the second invariant of deviatoric stress and $\bar{\epsilon}_p$ is the isotropic hardening parameter. The flow rule is given by the Prandtl-Reuss equation, which is obtained by considering the von Mises yield function (see Eq. 21) as the flow potential. The flow vector reads:

$$\mathbf{N} = \frac{\partial f}{\partial \boldsymbol{\sigma}} = \sqrt{\frac{3}{2}}\frac{\mathbf{s}}{||\mathbf{s}||} \tag{23}$$

Where $\mathbf{s}$ is the deviatoric stress tensor. Hardening is a phenomenological aspect of plastic yielding which is characterized by the dependence of the critical yield value on the history of plastic strains. For the current

framework, a rate-independent isotropic hardening is considered. It is incorporated into the formulation by making the yield stress as a function of accumulated plastic strain as given in Eq. 21 and corresponds to uniform expansion of initial yield locus. On the other hand, a perfectly plastic behavior is characterized with no hardening. The yield stress does not depend on the accumulated plastic strain. In the current framework, strain hardening approach is utilized to treat the isotropic hardening behavior. Taking into account the associative flow rule, the rate evolution equation can be formulated as

$$\bar{\epsilon} = \sqrt{\frac{2}{3}} ||\boldsymbol{\epsilon_p}|| \tag{24}$$

The implementation of the constitutive model is based on the book by Neto et. al. [24].

3.3.1 Implicit numerical integration scheme

Two essential material specific operations involved are: (1) the state update procedure, where stress σ_{n+1}^k and hardening variable $\bar{\epsilon}_p^k$ are computed at every Gauss point and (2) computing the tangent stiffness matrix for solving the nonlinear finite element equation (see Eq. 20). In the state update procedure presented here,

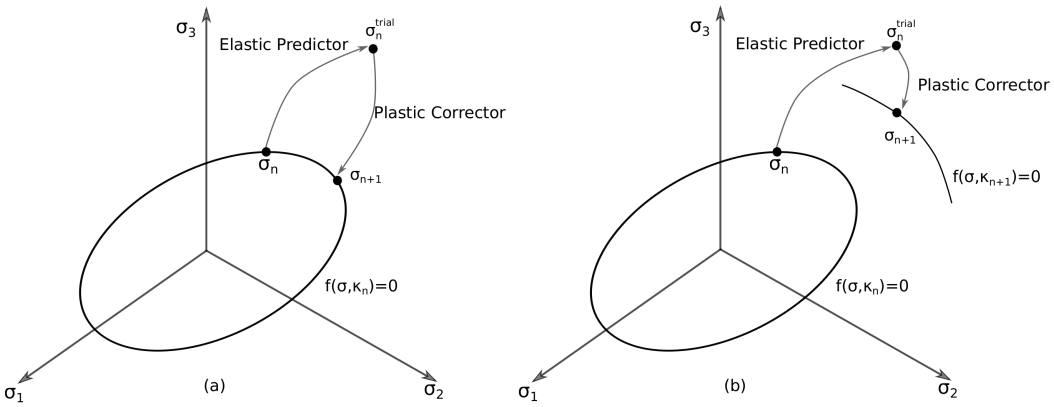

Figure 3: Geometrical illustration of Return-Mapping scheme: (a) perfect plasticity and (b) with hardening

backward Euler scheme is utilized. This leads to a two-step algorithm for the state update as follows:

1. Elastic Trial Step

   In a given increment $[t_n - t_{n+1}]$ with a strain increment $\Delta\epsilon$, solution is assumed to be elastic and leads to an elastic trial solution

   $$\epsilon_{n+1}^{e,trial} = \epsilon_n^e + \Delta\epsilon \tag{25}$$

   $$\bar{\epsilon}_{p_{n+1}} = \bar{\epsilon}_{p_n} \tag{26}$$

   The corresponding elastic trial stress is computed and solution is accepted, if the elastic trail stress lies within the yield locus. In case the elastic trial stress exceeds the yield locus, Plastic Corrector Step is initiated

2. Plastic Corrector Step

A scalar nonlinear equation with incremental plastic multiplier $\Delta\gamma$ as the unknown is solved using Newton-Raphson (NR) method

$$\bar{f}(\Delta\gamma) = q_{n+1}^{trial} - 3G\Delta\gamma - \sigma_y(\bar{\epsilon}_n^p + \Delta\gamma) \tag{27}$$

Where q_{n+1}^{trial} is the trial von Mises stress. With solution $\Delta\gamma$ at hand, state variables are updated

$$\mathbf{s}_{n+1} = \left(1 - \frac{\Delta\gamma 3G}{q_{n+1}^{trial}}\right)\mathbf{s}_{n+1}^{trial} \tag{28a}$$

$$\boldsymbol{\sigma}_{n+1} = \mathbf{s}_{n+1} + p_n^{trial}\mathbf{I} \tag{28b}$$

$$\boldsymbol{\epsilon}_{n+1}^e = \frac{1}{2G}\mathbf{s}_{n+1} + \frac{1}{3}\epsilon_v^{e,trial}\mathbf{I} \tag{28c}$$

$$\bar{\epsilon}_{n+1}^p = \bar{\epsilon}_{n+1}^p + \Delta\gamma \tag{28d}$$

Geometrical interpretation of return-mapping scheme is illustrated in Fig. 3. It should be noted that each iteration step consists of a global Newton-Raphson step for computing the global incremental solution and local Newton-Raphson step at every Gauss point to compute the incremental plastic multiplier as shown in Eq. 27. The elastoplastic tangent modulus ($\mathbf{C}^{ep}$) is obtained by taking variations of integrated equations with respect to the solution variables. An elastoplastic consistent tangent operator is defined as follows:

$$\mathbf{C}^{ep} = \frac{\partial\sigma}{\partial\epsilon_{n+1}^{e,trial}} \tag{29}$$

After straightforward manipulation of Eqs. 28-29, following expression can be obtained

$$\mathbf{C}_{ep} = \mathbf{C}_e - \frac{\Delta\gamma\, 6G^2}{q_{n+1}^{trial}}\mathbf{I}_d + 6G^2\left(\frac{\Delta\gamma}{q_{n+1}^{trial}} - \frac{1}{3G+H}\right)\bar{\mathbf{N}}_{n+1}\otimes\bar{\mathbf{N}}_{n+1} \tag{30}$$

Where G and H are the hardening and bulk modulus respectively [24]. The elastoplastic consistent tangent operator (see Eq. 30) is consistent with the implicit return-mapping scheme employed for state update procedure and is based on the works of Simo and Taylor [25]. Based on the consistent tangent material operator (Eq. 30), we can formulate the tangent fundamental nucleus for CUF as follows

$$k_{ij\tau s}^{tan} = \int_l\int_\Omega \mathbf{D}^T(N_i(y)F_\tau(x,z))\,\mathbf{C}_{ep}\,\mathbf{D}(N_j(y)F_s(x,z))dl\,d\Omega \tag{31}$$

The integrals for the FN are computed numerically using Gauss quadrature technique. Selective integration scheme was used to compute the integrals [1]. Additionally, the isotropic hardening curve ($\sigma_y(\bar{\epsilon}_p)$) is assumed to be piece-wise linear. The framework accepts a set of data points that approximate the arbitrarily nonlinear hardening curve. Linear interpolation is employed to approximate between the data points. This allows the use

of experimental hardening curve directly into the simulation.

4 Numerical Results

In this section, the capabilities of the non-linear CUF framework is illustrated through three numerical examples. First, an elastoplastic cantilever beam with compact cross-section under a bending load is investigated. An analytical solution is available for the proposed problem and the example serves a good benchmark to evaluate the performance of the refined-beam models. The second and third numerical examples investigate the refined capabilities of CUF models to analyze thin walled beams. A lipped channel beam and Z-beam is investigated and complex mechanical behaviors such as coupled bending-torsion and localized plasticity growth is efficiently analyzed by the CUF models. For each set of numerical examples, a classical 3D finite element model is built in ABAQUS and the results serve as a benchmark to assess the accuracy and efficiency of the refined beam models. Displacement profiles, 3D deformed configurations, accumulated plastic growth contours and stress contours are presented for validation purposes.

4.1 Compact Cantilever Beam

In the current example, a cantilever beam with rectangular cross-section under a vertical load at the center of the tip cross-section is investigated. The material and geometric properties of the beam are illustrated in Table 1 and the example is based on the work of Wen et al. [8]. An ideal elastic-perfect plastic stress-strain model is adopted, where the stress remains the same beyond the yield point.

Timoshenko and Gere developed an analytical solution for deflection of elastoplastic beam of rectangular cross-section under bending load [2]. The non-dimensional form of the solution is given as follows:

Elastic Region

$$\frac{\delta}{\delta_y} = \frac{P}{P_y} \qquad \left(0 \leq \frac{P}{P_y} \leq 1\right) \tag{32a}$$

Plastic Region

$$\frac{\delta}{\delta_y} = \left(\frac{P}{P_y}\right)^2 \left[5 - \left(3 + \frac{P}{P_y}\right)\sqrt{3 - \frac{2P}{P_y}}\right] \quad \left(1 \leq \frac{P}{P_y} \leq \frac{3}{2}\right) \tag{32b}$$

Where δ_y is the displacement at the yield load P_y. The equilibrium path is depicted in Fig. 4. The ratio between the limit load and yield load is termed as plastic strength factor. The geometry of the beam is illustrated in Fig. 5. The beam was discretized using B4 elements. The vertical load was applied at the tip of the beam in increments. The cross-section of the beam wass modeled using LE and TE models as illustrated in Fig. 5.

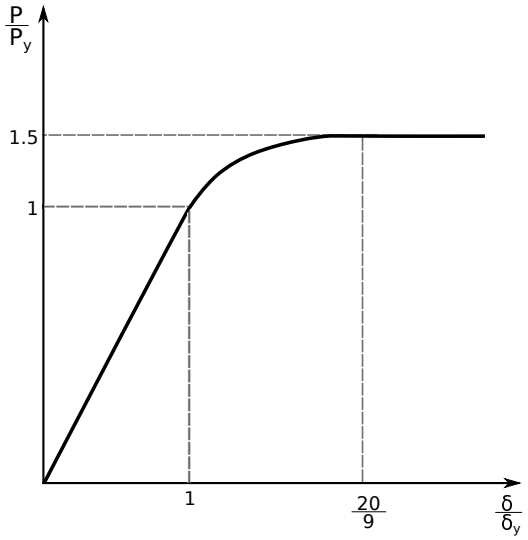

Figure 4: Equilibrium path for the compact cantilever beam [2]

Table 1: Geometric and material properties of the compact cantilever beam

Parameters	Values	Units
Geometrical Properties		
Beam Length (L)	50.0	m
Cross-section width (w)	1000.0	mm
Cross-section heigth (h)	800.0	mm
Material Properties		
Young modulus	210.0	GPa
Poisson Ratio	0.3	-
Yield Stress	210.0	MPa

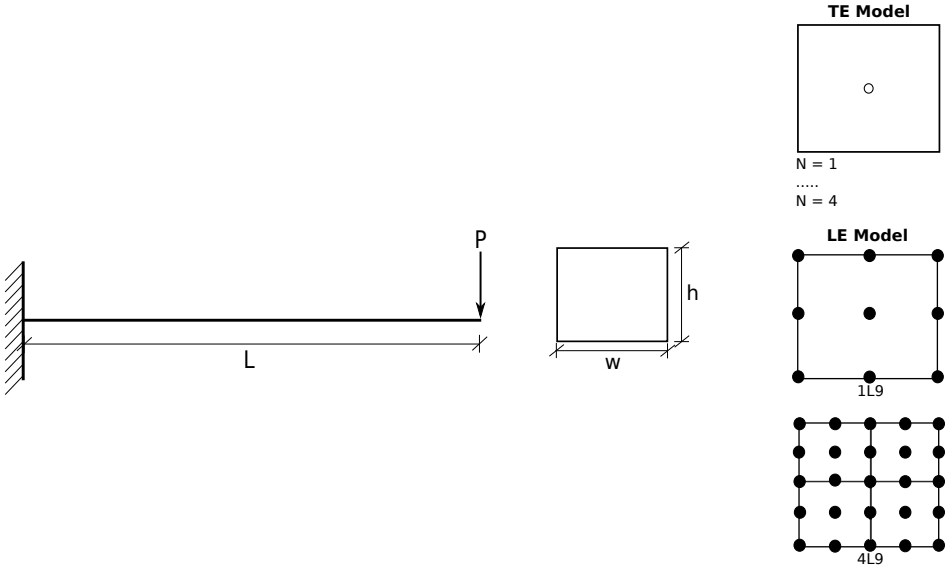

Figure 5: Geometry and cross-section modelings of the compact cantilever beam

The results from various models are tabulated in Table 2. The results are given in terms of vertical displacement at limit load and yield load and plastic strength factors. Classical models such as EBBT and TBT as well as refined beam models are compared against ABAQUS 3D solid results. Comparisons of equilibrium paths for various beam models are illustrated in Fig. 6. The convergence study for beams with various number of elements along the axis is tabulated in Table 3. The results suggest that,

Table 2: Comparison of displacement and plastic strength factors for various beam models, compact cantilever beam

Type	NDOF	u_z at yield force		u_z at limit load		Plastic Strength Factor	
		Value (m)	Error (%)	Value (m)	Error (%)	Value	Error (%)
Analytical	-	2.08	-	4.622	-	1.5	-
Secant Stiffness Form. [8]	-	-	-	4.82	4.28	1.51	0.67
ABAQUS							
3D Solid (Coarse)	22,590	2.067	0.62	4.281	7.38	1.55	3.57
3D Solid (Refined)	148,797	2.077	0.14	4.467	3.35	1.54	2.38
Classical Models							
EBBT	183	2.083	0.16	6.406	38.60	3.08	105.00
TBT	305	2.084	0.18	6.407	38.61	3.08	105.00
TE							
N = 1	549	2.084	0.18	6.407	32.38	3.08	105.00
N = 2	1098	2.079	0.07	4.937	6.81	1.55	3.33
N = 3	1830	2.079	0.06	4.735	2.44	1.53	2.00
N = 4	2745	2.079	0.06	4.624	0.03	1.52	1.29
LE							
1L9	1647	2.0787	0.06	3.623	21.61	1.35	10.00
4L9	4575	2.0789	0.05	4.534	1.90	1.52	1.29

1. All models provide accurate results within the elastic regime. On the other hand, classical beam models fail, when the load exceeds the elastic limit.

2. Higher-order CUF 1D models can capture plastic behavior very accurately at a very reduced computational cost as compared to the ABAQUS 3D solution.

3. From Table 3, it is evident how the further refinement of CUF models leads to increased accuracy in results

4.2 Lipped Channel Beam

The problem statement is based on the work of Abambres et al. [10]. The geometry and boundary conditions of the beam are illustrated in Fig. 7. Two vertical line loads of $\lambda N/mm$ were applied at the mid-span of the beam along the top and bottom flanges. The material behavior is modeled as isotropic with a Young modulus, $E = 200GPa$, Poisson ratio, $\nu = 0.3$ and nominal yield stress, $\sigma_y = 450MPa$. A perfect plastic case is considered with strain-hardening slope $H = 0$. TE and LE models were used to model the problem as illustrated in Fig. 8. The model was also developed in ABAQUS using shell elements (full integration with 5

Table 3: Convergence study of various refined beam models for the compact cantilever beam

Type	NDOF	Displacement at yield force		Displacement at limit load		Plastic Strength Factor	
		Value (m)	Error (%)	Value (m)	Error (%)	Value	Error (%)
B4 - 10 elements							
TE							
EBBT	93	2.0833	0.16	6.501	40.64	3.10	106.67
TBT	155	2.0837	0.18	6.502	40.68	3.10	106.67
N=1	279	2.0837	0.18	6.502	40.68	3.10	106.67
N=2	558	2.0717	0.40	5.052	9.30	1.57	4.33
N=3	930	2.0719	0.39	4.852	4.97	1.56	3.67
N=4	1395	2.0719	0.39	4.729	2.30	1.55	3.00
LE							
1L9	837	2.0718	0.39	3.062	33.76	1.35	10.00
4L9	2325	2.0719	0.39	4.514	2.34	1.52	1.66
B4 - 20 elements							
TE							
EBBT	183	2.0833	0.16	6.407	38.60	3.08	105.00
TBT	305	2.0837	0.18	6.408	38.64	3.08	105.00
N=1	549	2.0837	0.18	6.408	38.64	3.08	105.00
N=2	1098	2.0770	0.14	4.909	6.20	1.55	3.33
N=3	1830	2.0772	0.13	4.695	1.58	1.54	2.67
N=4	2745	2.0772	0.13	4.659	0.77	1.53	2.00
LE							
1L9	1647	2.0771	0.14	3.623	21.61	1.35	10.00
4L9	4575	2.0773	0.13	4.534	1.90	1.52	1.29
B4 - 30 elements							
TE							
EBBT	273	2.0833	0.16	6.407	38.60	3.08	105.00
TBT	455	2.0837	0.18	6.408	38.61	3.08	105.00
N=1	819	2.0837	0.18	6.408	38.63	3.08	105.00
N=2	1638	2.0786	0.07	4.937	6.81	1.55	3.33
N=3	2730	2.0788	0.06	4.735	2.44	1.53	2.00
N=4	4095	2.0788	0.06	4.624	0.03	1.52	1.33
LE							
1L9	2457	2.0787	0.06	3.579	22.56	1.35	10.00
4L9	6825	2.0789	0.05	4.591	0.69	1.52	1.32

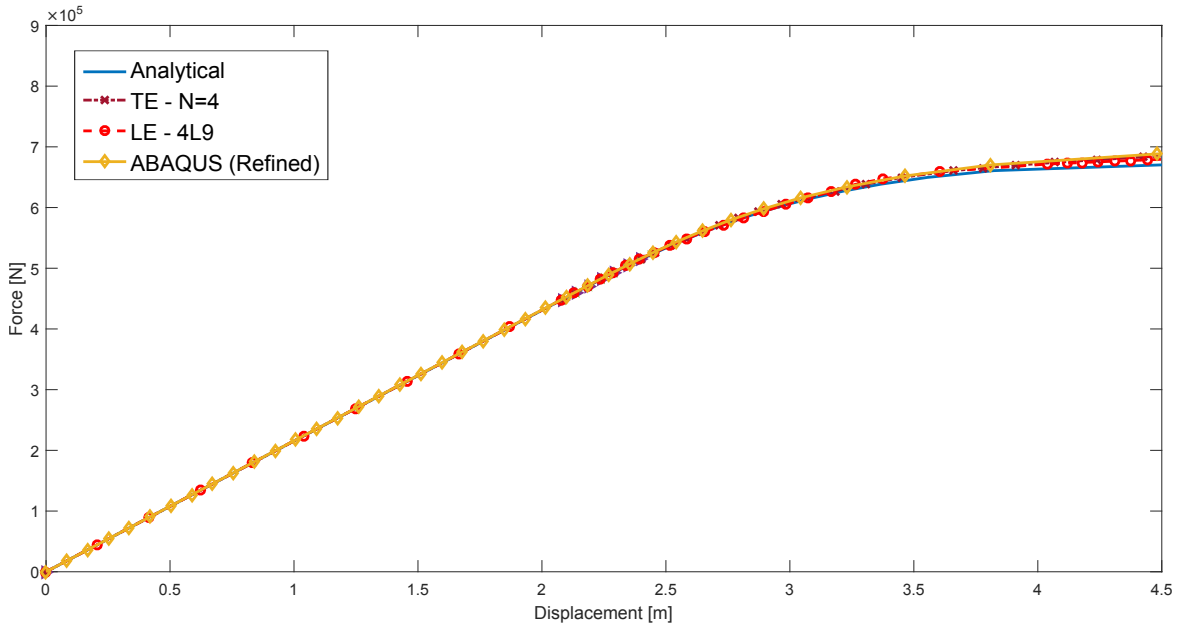

Figure 6: Equilibrium path of various beam models for the compact cantilever beam (30 B4 elements used for TE and LE models)

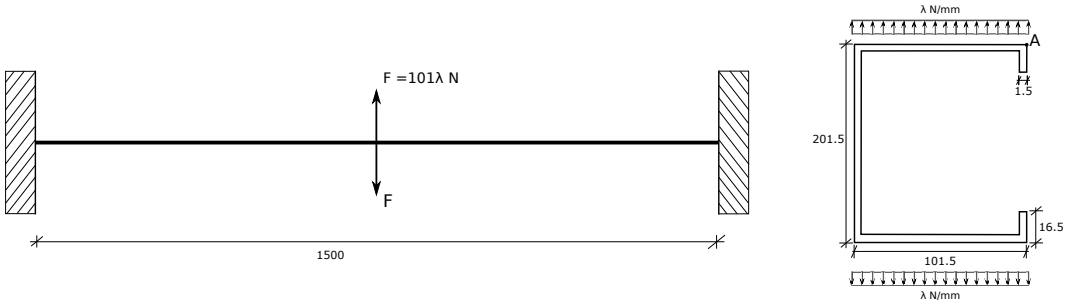

Figure 7: Geometry of the lipped channel beam

Gauss points through the thickness) and 3D linear elements (linear elements with full integration) with degrees of freedom of 69,948 and 1,342,656 respectively [26]. The displacements were evaluated at point A (see Fig. 7) at two load points: (1) $\lambda = 12.69$ (elastic regime) and (2) $\lambda = 40.94$ (elasto-plastic regime), henceforth referred to as elastic and elasto-plastic point respectively. Table 4 comprises the computed displacement at point A (see Fig. 7) for various beam models. The results are compared against reference solution obtained from the work of Abambres et al [10] and ABAQUS solutions. Results from EBBT and TBT were not reported because this load configuration would result in null displacements. In fact, both models can deal with rigid, transverse displacements. The 3D deformation configuration obtained from LE-44L9 model and ABAQUS 3D model is illustrated in Fig. 10. The displacement profile (U_z) at point A along the length of the beam is depicted in Fig. 9. Figures 11-13 consists of contour plots at the elasto-plastic point for von Mises stress (σ_{vm}) distribution, equivalent plastic strain ($\bar{\epsilon_p}$) distribution, and shear stress (σ_{xy}) distribution. The results suggest that,

1. The ability of CUF beam models, especially LE models, to detect accurate displacement and stress fields for thin walled beams has been successfully employed to account for plasticity in analysis

2. From Fig. 9, it is evident that displacement profiles for 44L9 and ABAQUS 3D model are similar and within the acceptable limits.

3. Local accumulation of plasticity can be observed at mid-span of the beam along the tip of the lip, flange and web-flange intersection. Also, local effects nearby the loading area are perfectly detected.

4. From Table 4, it is evident that continued enrichment of the displacement field improve results. LE-44L9 model requires only about 5.42% of the total degrees of freedom of that of an ABAQUS 3D model to provide similar results. It is important to underline that uniform meshes and cross-section discretizations were adopted in this paper. The number of degrees of freedom can be decreased further by employing different sets of cross-sectional meshes along the beam axis and cross-section.

5. LE models are more efficient than TE because of their capability to locally refine the displacement field via the use of more cross-sectional elements.

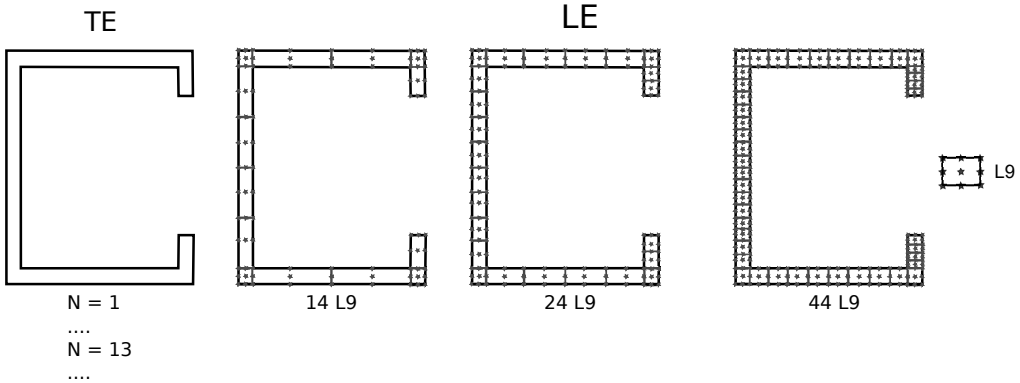

Figure 8: TE and LE models for the lipped channel beam

Table 4: Vertical displacement at point A for various models for the fixed-ended lipped channel beam

	NDOF	Displacement (u_z)	
		$\lambda = 12.69$	$\lambda = 40.94$
GBT[10]	3,222	13.63	77.6
ABAQUS - Shell	69,948	13.47	74.93
ABAQUS - 3D Brick	1,342,656	13.31	69.92
B4-10 elements			
TE			
EBBT	-	-	-
TBT	-	-	-
N=1	279	0.002	0.006
N=2	558	0.004	0.120
N=3	930	0.011	0.036
N=4	1,395	0.088	0.285
N=5	1,953	0.139	0.448
N=6	2,604	1.724	5.699
N=7	3,348	2.344	8.308
N=8	4,185	7.632	28.324
N=9	5,115	9.411	36.542
N=10	6,138	10.262	42.096
N=11	7,254	11.221	48.179
N=12	8,463	11.768	53.037
LE			
14L9	8,091	13.143	68.110
24L9	13,671	13.270	69.630
44L9	24,831	13.300	70.850
B4-20 elements			
TE			
N=1	549	0.002	0.006
N=2	1,098	0.004	0.012
N=3	1,830	0.011	0.036
N=4	2,745	0.088	0.285
N=5	3,843	0.139	0.448
N=6	5,124	1.724	5.713
N=7	6,588	2.345	8.315
N=8	8,235	7.638	29.076
N=9	10,065	9.421	37.621
N=10	12,678	10.273	12.678
N=11	14,274	11.234	49.376
N=12	16,653	11.783	54.473
LE			
14L9	15,921	13.160	71.910
24L9	26,901	13.280	74.156
44L9	48,861	13.320	76.009
B4-30 elements			
TE			
N=1	819	0.002	0.006
N=2	1,638	0.004	0.012
N=3	2,730	0.011	0.036
N=4	4,095	0.088	0.285
N=5	5,733	0.139	0.448
N=6	7,644	1.725	5.708
N=7	9,828	2.345	8.317
N=8	12,285	7.640	29.004
N=9	15,015	9.424	37.619
N=10	18,018	10.277	43.409
N=11	21,294	11.238	50.266
N=12	24,843	11.786	55.495
LE			
14L9	23,751	13.170	73.220
24L9	40,131	13.285	75.947
44L9	72,891	13.321	78.340

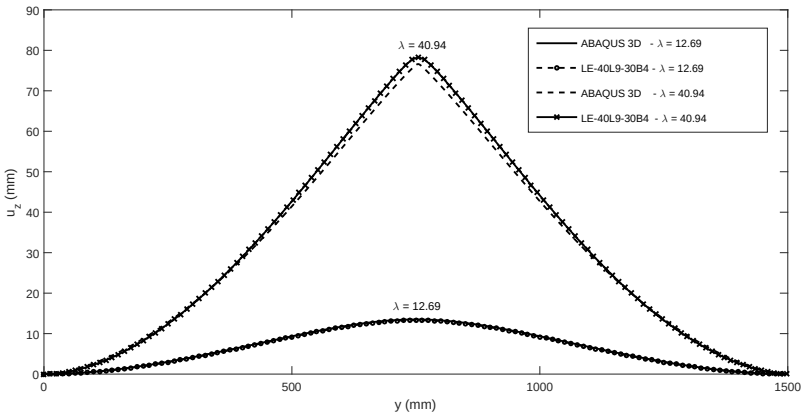

Figure 9: Displacement profile (u_z) along y for the fixed-ended lipped channel beam

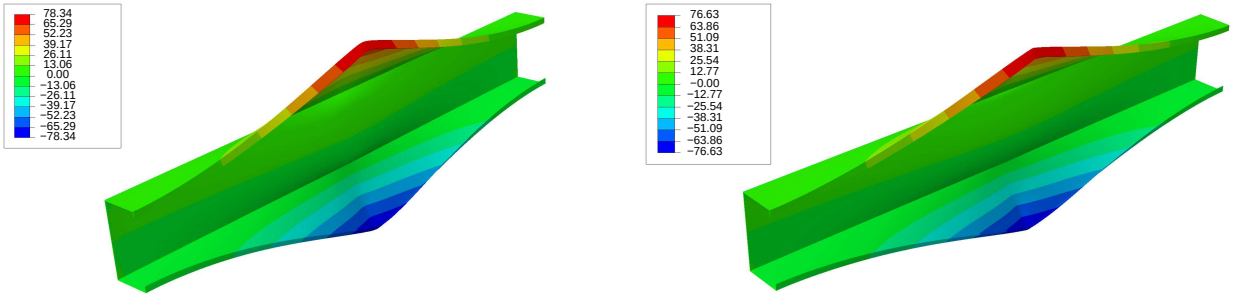

(a) LE-44L9 **(b)** ABAQUS 3D

Figure 10: Deformed configuration (u_z) at $\lambda = 40.98$ for the fixed-ended lipped channel beam

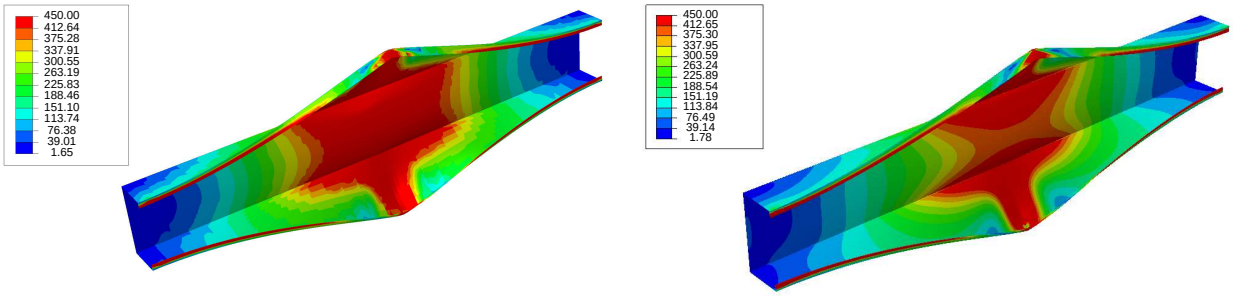

(a) LE-44L9 **(b)** ABAQUS 3D

Figure 11: von Mises stress distribution at $\lambda = 40.98$ for the fixed-ended lipped channel beam

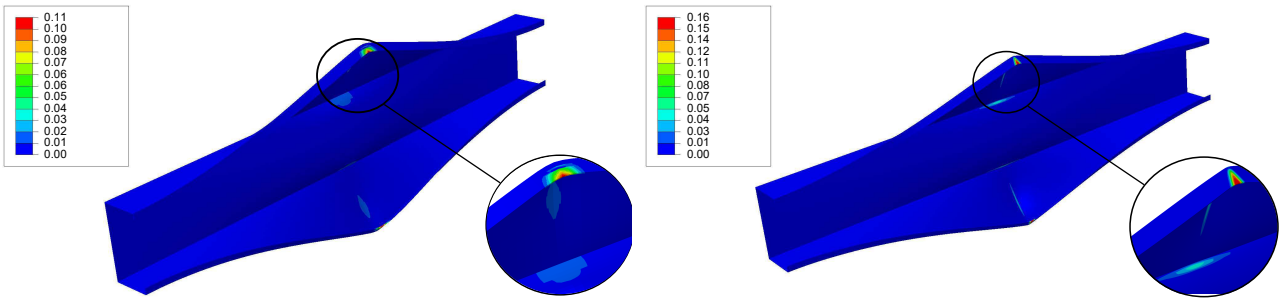

(a) LE-44L9 **(b)** ABAQUS 3D

Figure 12: Equivalent plastic strain distribution at $\lambda = 40.98$ for the fixed-ended lipped channel beam

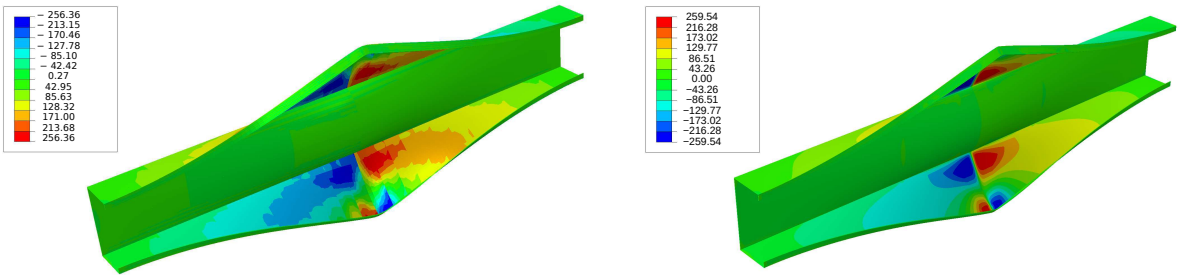

(a) LE-44L9 **(b)** ABAQUS 3D

Figure 13: Shear stress distribution σ_{xy} at $\lambda = 40.98$ for the fixed-ended lipped channel beam

4.3 Z-beam under pressure load

A clamped-clamped Z-beam is considered with length L = 1000 mm as depicted in Fig. 14. The pressure load acts in opposite directions. The cross-section of the beam is modeled using TE and LE models are depicted in Fig. 15. The material behavior of Aluminium is assumed with a Young modulus, $E = 70\,GPa$, Poisson ratio, $\nu = 0.3$ and nominal yield stress, $\sigma_y = 300\,MPa$. An isotropic elastoplastic is considered with isotropic hardening as in Table 5.

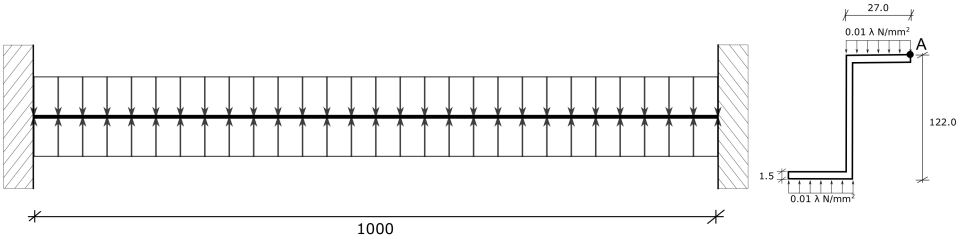

Figure 14: Geometry of the Z-Beam

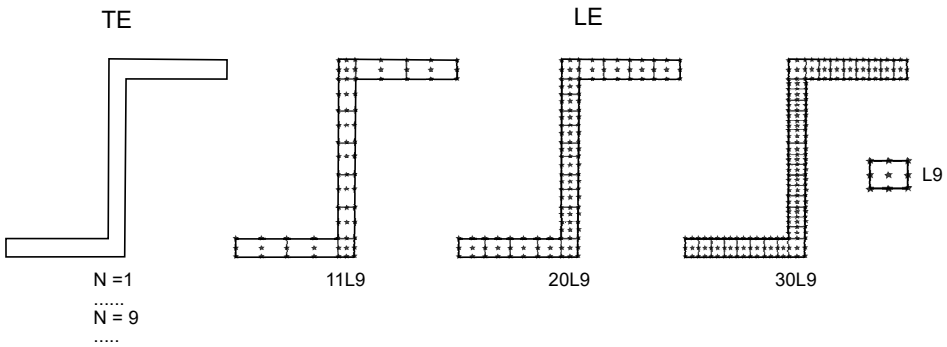

Figure 15: TE and LE models for clamped Z-Beam

Table 5: Isotropic hardening data for the Z-beam problem [27]

Stress (MPa)	300	320	340	355	375	390	410	430	450	470	484
Plastic Strain	0.000	0.0002	0.00047	0.0012	0.0045	0.01036	0.0213	0.0344	0.0513	0.0800	0.147

A similar model was developed in ABAQUS using shell elements (full integration with 5 Gauss points through the thickness) and 3D linear elements (linear elements with full integration) with degrees of freedom 42,210 and

697,392, respectively [26]. Two load points are considered for the result evaluation: (1) $\lambda = 12$ (elastic regime) and (2) $\lambda = 50$ (elasto-plastic regime), henceforth referred to as elastic and elasto-plastic point respectively. The displacement u_x and u_z is evaluated at point A and tabulated for different beam models in Table 6. Contour plots of the LE-30L9 with 30 B4 elements models are compared against the reference ABAQUS 3D solutions. All the contour plots are evaluated at elasto-plastic point. The displacement profile (u_x) at point A along the beam is given in Fig. 16. 3D deformation configuration of the beam at elasto-plastic point for u_x and u_z are depicted in Fig. 17 and Fig. 18 respectively. von Mises stress (σ_{vm}) distribution, equivalent plastic strain ($\bar{\epsilon_p}$) distribution and transverse stress (σ_{xy}) distribution are depicted in Figs. 19-21.

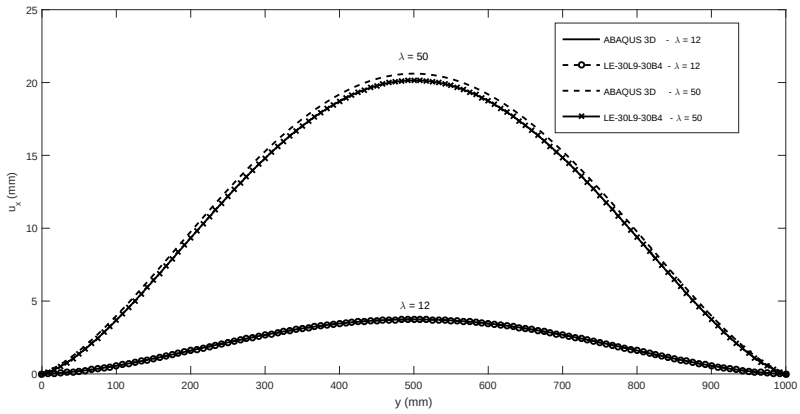

Figure 16: Displacement profile (u_x) along y, Z-beam

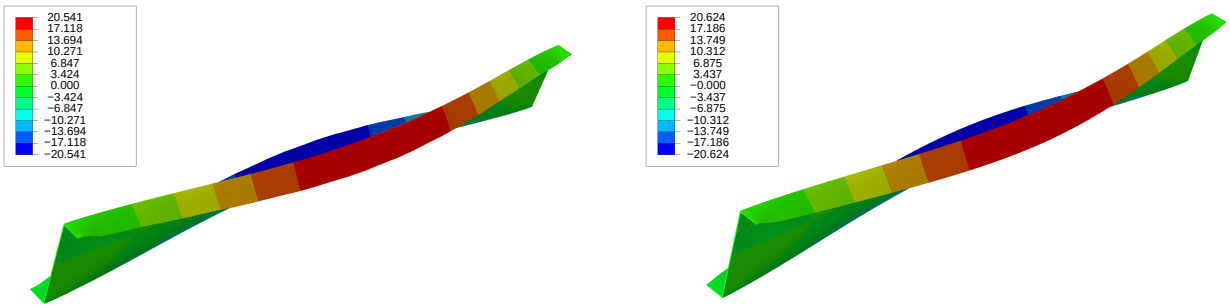

(a) LE-30L9 **(b)** ABAQUS 3D

Figure 17: Deformed configuration (u_x) at $\lambda = 50$, Z-beam

The results suggest that,

1. Local accumulation of plastic growth can be observed at the clamped ends of the beam and the flange end.

2. TE models provide reasonably good results in this case. In fact, the presence of a distributed load makes the severity of local effects weaker. Therefore, the need for local refinements is less fundamental.

3. Even the less-refined LE models (11L9) can capture the deformation mechanism quite accurately. It requires less than 2% of the total degrees of freedom of a 3D ABAQUS model to provide an accuracy

Table 6: Displacement for various beam configurations, Z-beam

Type	NDOF	Displacement at $\lambda = 12$		Displacement at $\lambda = 50$	
		u_x	u_z	u_x	u_z
ABAQUS 3D	697,392	3.74	3.046	20.62	14.85
ABAQUS 2D	42,210	3.79	2.803	21.02	13.89
B4 - 10 elements					
TE					
N=1	279	0.045	0.021	0.186	0.086
N=2	558	0.466	0.202	1.942	0.841
N=3	930	0.476	0.207	1.981	0.864
N=4	1,395	2.710	1.173	11.589	5.015
N=5	1,953	2.736	1.312	11.765	5.613
N=6	2,604	3.436	1.694	15.958	7.775
N=7	3,348	3.425	2.025	15.852	9.101
N=8	4,185	3.642	2.164	17.756	10.131
N=9	5,115	3.646	2.417	17.458	11.045
LE					
11L9	6,417	3.703	2.786	17.902	12.673
20L9	11,439	3.704	2.835	17.930	12.880
33L9	18,693	3.705	2.852	17.940	12.962
B4 - 20 elements					
TE					
N=1	549	0.045	0.021	0.186	0.086
N=2	1,098	0.466	0.202	1.943	0.841
N=3	1,830	0.477	0.208	1.987	0.866
N=4	2,745	2.723	1.178	11.857	5.129
N=5	3,843	2.750	1.318	12.058	5.734
N=6	5,124	3.457	1.703	17.103	8.266
N=7	6,588	3.446	2.033	17.023	9.592
N=8	8,235	3.665	2.174	19.114	10.714
N=9	10,065	3.669	2.427	19.066	11.733
LE					
11L9	12,627	3.726	2.796	19.599	13.399
20L9	22,509	3.728	2.845	19.627	13.609
33L9	36,783	3.727	2.869	19.710	13.758
B4 - 30 elements					
TE					
N=1	819	0.045	0.021	0.186	0.086
N=2	1,638	0.466	0.202	0.186	0.086
N=3	2,730	0.477	0.208	0.186	0.086
N=4	4,095	2.727	1.180	1.943	0.841
N=5	5,733	2.755	1.319	1.988	0.867
N=6	7,644	3.463	1.706	12.035	5.206
N=7	9,828	3.452	2.036	18.089	10.041
N=8	12,285	3.672	2.177	20.445	11.288
N=9	15,015	3.676	2.430	20.577	12.379
LE					
11L9	18,837	3.733	2.799	20.056	13.596
20L9	33,579	3.735	2.848	20.160	13.840
33L9	54,873	3.735	2.886	20.541	14.223

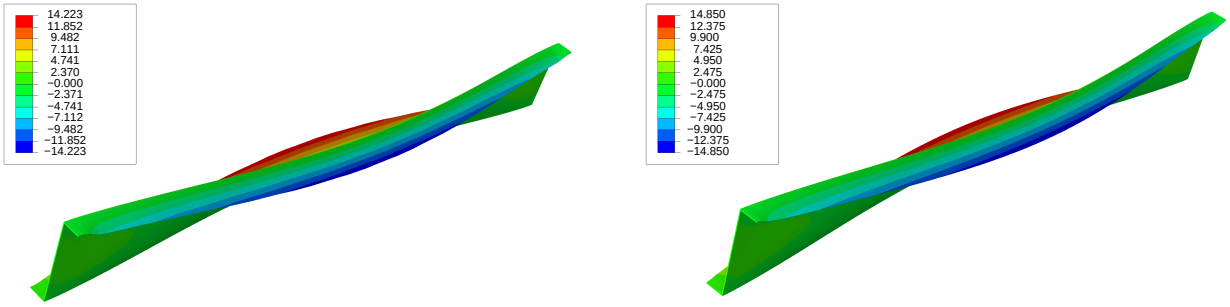

(a) LE-30L9 **(b)** ABAQUS 3D

Figure 18: Deformed configuration (u_z) at $\lambda = 50$, Z-beam

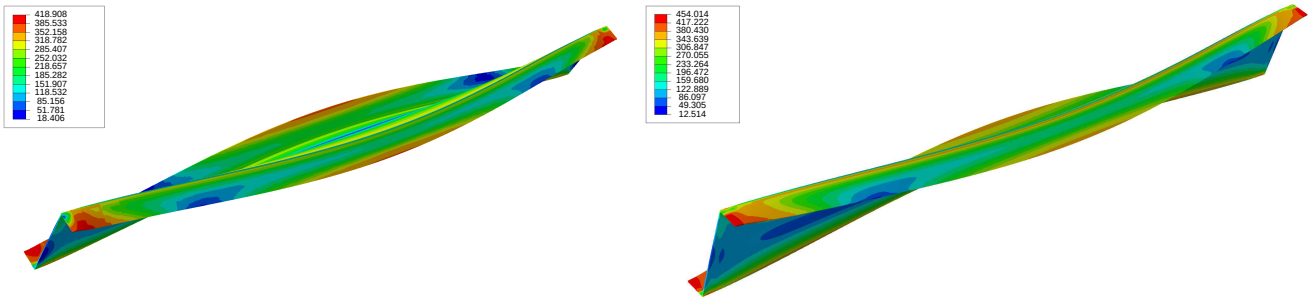

(a) LE-30L9 **(b)** ABAQUS 3D

Figure 19: von nMises stress distribution at $\lambda = 50$, Z-beam

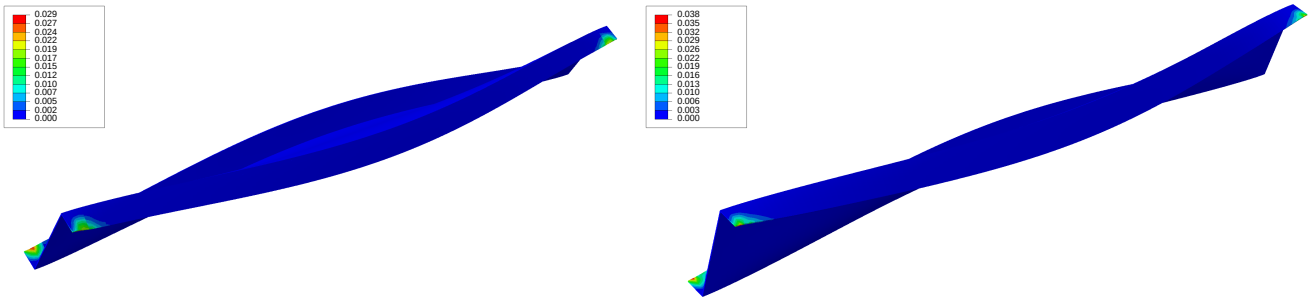

(a) LE-30L9 **(b)** ABAQUS 3D

Figure 20: Equivalent plastic strain distribution at $\lambda = 50$, Z-beam

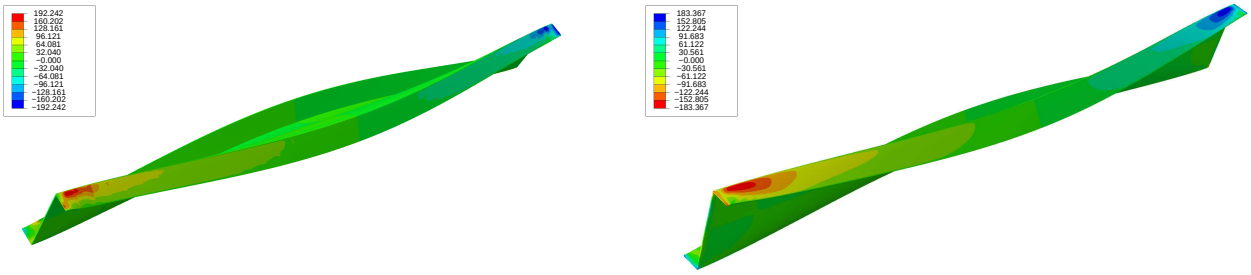

(a) LE-30L9 **(b)** ABAQUS 3D

Figure 21: Shear stress (σ_{xy}) distribution at $\lambda = 50$, Z-beam

within 7%.

4. LE-30L9 model requires only about 7.8% of the total degrees of freedom of that of an ABAQUS 3D model to provide similar displacement and stress fields.

5 Conclusion

A computationally efficient framework for physically non-linear structural simulations based on refined beam model is presented. The von Mises plasticity theory was incorporated along with Carrera Unified Formulation (CUF) to undertake non-linear finite element analyses. The isotropic non-linear strain-hardening was integrated into the constitutive model to account for material non-linearity. Using the principle of virtual work, the nonlinear governing equations and related finite element approximations were formulated. A Newton-Raphson based linearized increment scheme was employed to solve the system of nonlinear algebraic equations. 1D modeling approaches based on TE (Taylor Expansion) and LE (Lagrange Expansion) were considered to model the cross-section displacement field. Compact and thin walled structures were considered under local and distributed loads. Comparisons were carried out against data from literature, shell and solid finite elements. The following conclusions can be drawn:

1. Classical beam models can be very inaccurate in the non-linear regime.

2. 1D structural models can detect 3D-like effects. However, the use of refined 1D model is mandatory to deal with local effects and cross-sectional distortions.

3. The present LE models are particularly efficient to deal with thin-walled structures under local loadings. Also, the use of LE models allows us to assign the material characteristics at local level along the cross-section of the beam via the use of the cross-section Lagrange elements.

4. TE models can be used as soon as distributed loads are considered.

5. The amount of degrees of freedom of 1D refined models is, at least, ten times smaller than 3D solid elements.

Future works will deal with the development of models for the material and geometrical non-linear analysis.

6 Acknowledgment

This research work has been carried out within the project FULLCOMP (FULLy analysis, design, manufacturing, and health monitoring of COMPosite structures), funded by the European Union Horizon 2020 Research and Innovation program under the Marie Skłodowska-Curie grant agreement No. 642121.

References

[1] Carrera E., Cinefra M., Petrolo M., and Zappino E. *Finite Element Analysis of Structures through Unified Formulation*. John Wiley and Sons, Ltd, 2014.

[2] Timoshenko S.P. and Gere J.M. *Mechanics of Materials*. Springer-Science+Business Media, B.V., 1991.

[3] Orbison J.G., McGuire W., and Abel J.F. Yield surface application in nonlinear steel frame analysis. *Computer Methods in Applied Mechanics and Engineering*, 33:557–573, 1982.

[4] Mata P., Oller S., and Barbat A.H. Static analysis of beam structures under nonlinear geometric and constitutive behavior. *Computer Methods in Applied Mechanics and Engineering*, 196:4458–4478, 2007.

[5] Corradi L. and Poggi C. A refined finite element model for the analysis of elastic-plastic frames. *International Journal for Numerical Methods in Engineering*, 20:2155–2174, 1984.

[6] Shi G. and Atluri S. N. Elasto-plastic large deformation analysis of space-frames: A plastic-hinge and stress-based explicit derivation of tangent stiffnesses. *International Journal for Numerical Methods in Engineering*, 26:589615, 1988.

[7] Davenne L., Ragueneau F., Mazars J., and Ibrahimbegovic A. Efficient approaches to finite element analysis in earthquake engineering. *Computers and Structures*, 81:12231239, 2003.

[8] Y. Wen and Q.Y. Zeng. A novel approach to elasto-plastic finite element analysis of beam structures using the concept of incremental secant stiffness. *Finite Element in Analysis and Design*, 46:982–991, 2010.

[9] Chen W. F. and Toma S. Advanced Analysis of Steel Frames. *CRC Press*, 1994.

[10] Abambres M., Camotim D., and Silvestre N. GBT-based first-order analysis of elastic-plastic thin-walled steel members exhibiting strain-hardening. *The IES Journal Part A: Civil & Structural Engineering*, 6(2):119–134, 2013.

[11] Abambres M., Camotim D., and Silvestre N. GBT-based structural analysis of elasticplastic thin-walled members. *Computer and Structures*, 136:1–23, 2014.

[12] Gonalves R. and Camotim D. Geometrically non-linear generalised beam theory for elastoplastic thin-walled metal members. *Thin-Walled Structures*, 51:121129, 2012.

[13] Carrera E. and Giunta G. Refined Beam Theories based on a Unified Formulation. *International Journal of Applied Mechanics*, 2:117–143, 2010.

[14] Carrera E. and Petrolo M. Refined Beam Elements with only Displacement Variables and Plate/Shell Capabilities. *Meccanica*, 47:537–556, 2011.

[15] Carrera E., Maiarú M., and Petrolo M. Component-wise analysis of laminated anisotropic composites. *International Journal of Solids and Structures*, 49:1839–1851, 2012.

[16] Giunta G., Biscani F., Belouettar S., and Carrera E. Analysis of Thin-Walled Beams via A One-Dimensional Unified Formulation through A Navier-Type Solution. *International Journal of Applied Mechanics*, 3(3):407–434, 2011.

[17] Ibrahim S.M., Carrera E., Petrolo M., and Zappino E. Buckling of composite thin walled beams by refined theory. *Composite Structures*, 94:563570, 2012.

[18] Pagani A., Miguel A.G. de, Petrolo M., and Carrera E. Analysis of laminated beams via Unified Formulation and Legendre polynomial expansions. *Composite Structures*, In-Press.

[19] Pagani A. and Carrera E. Unified formulation of geometrically nonlinear refined beam theories. *Mechanics of Advanced Materials and Structures*, 2016.

[20] Carrera E., Pagani A., Petrolo M., and Zappino E. Recent developments on refined theories for beams with applications. *The Japan Society of Mechanical Engineers*, 2:1–30, 2015.

[21] Carrera E., Cinefra M., Li G., and Kulikov G.M. MITC9 shell finite elements with miscellaneous through-the-thickness functions for the analysis of laminated structures. *Composite Structures*, 154:360373, 2016.

[22] von Mises R. Mechanics of solid bodies in the plastically-deformable state. *Mechanik der festen Körper in plastisch-deformablen Zustand*, 4:582–592, 1913.

[23] Bathe K.J. *Finite element procedure.* Prentice hall, USA, 1996.

[24] Neto E.A.de S., Peric D., and Owen D.R.J. *Computational Methods for Plasticity: Theory and Application.* John Wiley and Sons, Ltd, 2008.

[25] Simo J.C. and Taylor R.L. Consistent tangent operators for rate-independent elastoplasticity. *Computer Methods in Applied Mechanics and Engineering*, 48(1):101–118, 1985.

[26] ABAQUS. *Abaqus Analysis User's Guide.* Dassault Systmes, 2014.

[27] Lapczyk I. and J. A. Hurtado. Progressive damage modeling in fiber-reinforced materials. *Composites Part A: Applied Science and Manufacturing*, 38(11):2333–2341, 2007.